

Twinning mediated intralayer frustration governs structural degradation in layered Li-rich oxide cathode

Received: 4 August 2024

Accepted: 19 June 2025

Published online: 17 July 2025



Tingting Yang^{1,2,6}, Maolin Yang^{1,6}, Zhongyuan Huang¹, Rui Wang³, Wenhai Ji⁴, Peng-Han Lu², Tao Zeng¹, Zenan Li⁵, Jun Wang⁵, Rafal E. Dunin-Borkowski², Lei Jin²✉ & Yinguo Xiao¹✉

Layered Li-rich Mn-based (LRM) oxides are promising cathode materials for next-generation high-energy batteries. However, their commercialization is hindered by intrinsic structural issues and subsequent degradation processes. In order to address the degradation mechanisms, we use *operando* neutron diffraction and scanning transmission electron microscopy to follow the microstructural degeneration of the LRM oxides in a prepared full cell with a graphite anode. The methods enable both real-time phase analysis and structural evolution mapping across a wide field of view. The LRM oxide is observed to initially have a partially ordered Li_2MnO_3 -like structure with multiple planar defects. It transitions from an ordered monoclinic phase to a disordered rhombohedral phase as a result of irreversible Li^+ migration and transition metal rearrangement during cycling. Especially after the first full charge, the interlayer (001) twinning-like structures and local intralayer frustrations formed. Over cycling, the intralayer frustrations further develop into pore-like microstructures along the {012} twinning boundary in the bulk of the particles, which contributes significantly to performance reduction. The results clarify the link between microstructure degradation and performance loss and provide valuable insights into the optimization of high-performance cathodes.

The stability of the primary framework structure of an intercalation compound profoundly influences the reversibility of its structural evolution during ion insertion and extraction^{1–4}. Practical applications of layered cathode materials for Li-ion batteries, such as Li-rich Mn-based (LRM) cathodes, require heightened stability of their transition metal (TM) layer framework due to the exceptional number of intercalated ions that they can accommodate^{5–7}. Although LRM cathode materials have an impressive energy density

of $\sim 900 \text{ Wh kg}^{-1}$ due to their high working voltage and substantial ion intercalation and deintercalation capacity^{8,9}, anion oxidation^{10,11}, oxygen release^{12,13}, irreversible damage from ion intercalation^{5,14,15} and complex interface reactions induced by a high cutoff voltage^{16,17} pose severe challenges for practical applications of LRM cathodes. Despite numerous studies on surface modification strategies to mitigate oxygen release, voltage decay remains a significant issue^{18–20}.

¹School of Advanced Materials, Peking University, Shenzhen Graduate School, Shenzhen 518055, PR China. ²Ernst Ruska-Centre for Microscopy and Spectroscopy with Electrons, Forschungszentrum Jülich GmbH, Jülich 52425, Germany. ³Department of Engineering, University of Cambridge, Cambridge CB30FS, UK. ⁴Spallation Neutron Source Science Center, Dongguan 523803, PR China. ⁵School of Innovation and Entrepreneurship, Southern University of Science and Technology, Shenzhen 518055, PR China. ⁶These authors contributed equally: Tingting Yang, Maolin Yang. ✉e-mail: ljin@fz-juelich.de; y.xiao@pku.edu.cn

Studies of the failure mechanisms of LRM cathodes must focus on both interface structure and bulk structure. By employing high-precision resonant inelastic X-ray scattering and ^{17}O solid-state nuclear magnetic resonance techniques, House et al. found that O_2 can form in a typical $\text{Li}_{1.2}\text{Ni}_{0.13}\text{Co}_{0.13}\text{Mn}_{0.54}\text{O}_2$ cathode and stay in the lattice during charging²¹. Density functional theory calculations showed that TM layer rearrangement during Li^+ deintercalation creates vacancy clusters and alters the charge compensation mechanism during discharge, contributing to voltage decay. Similar O vacancy migration behavior has been observed in $\text{Li}_{1.18}\text{Mn}_{0.53}\text{Ni}_{0.21}\text{Co}_{0.08}\text{O}_2$ layered cathodes using scanning transmission soft X-ray microscopy and X-ray electron layer diffraction imaging²². However, these studies focused on the O electronic structure and did not track TM^{n+} movement. Unfortunately, current research often relies on assumptions and inferences obtained from LRM cathode microstructures examined under specific conditions that do not reflect operational environments^{23–25}. The lack of systematic research on failure structures in LRM cathodes means that the structural evolution of LRM cathodes over their full lifecycles remains elusive.

In order to elucidate the true structural evolution of LRM cathode materials, the present study combines *operando* neutron diffraction, which has high sensitivity to both light elements and adjoining TMs, with four-dimensional scanning transmission electron microscopy (4D-STEM), phase analysis and atomic-resolution aberration-corrected electron microscopy, which provide complementary information about long and short-range structure. Such a multiscale approach reveals the initial lattice structure, TM layer rearrangement, phase and structure evolution, defect growth and structural failure.

Results

Structure of the pristine LRM cathode

The failure mechanism of a representative LRM cathode material of nominal composition $\text{Li}_{1.2}\text{Ni}_{0.13}\text{Co}_{0.13}\text{Mn}_{0.54}\text{O}_2$ was studied during an

electrochemical process. A protective spinel layer was introduced onto the surface of the LRM oxide during synthesis, as shown in Supplementary Fig. 1a, b, to ensure consistent electrochemical performance in a pouch cell. The morphology of the untreated LRM oxide (u-LRM) was shown in Supplementary Fig. 1c, d. Supplementary Fig. 2 shows that the electrochemical performance u-LRM cathode and synthesized LRM, which indicates that u-LRM exhibits a significantly lower initial Coulombic efficiency (ICE) compared to the surface-reconstructed sample (85% vs. 91%), suggesting a higher extent of irreversible oxygen redox reactions in the u-LRM. The results also show distinctive electrochemical characteristics in half-cell assessments, such as a characteristic O redox plateau during the initial charge cycle, voltage hysteresis during discharge and subsequent cycle-induced voltage decay²⁶.

Neutron powder diffraction (NPD) and Rietveld refinement reveal that the pristine LRM oxide comprises 97.27% of an $\text{O}3'$ phase (space group: $C2/m$), and 2.73% of a spinel phase (denoted S, space group: $Fd\bar{3}m$) (Fig. 1a). Comprehensive structural information is provided in Supplementary Table 1. Additionally, the residual negative scattering signal observed at the tetrahedral sites in the Fourier difference map (Supplementary Fig. 3) of the $\text{O}3'$ phase from the neutron diffraction pattern indicates Li^+ occupation at tetrahedral sites, aligning with spinel structure features and corroborating the existence of the spinel phase in LRM. 4D-STEM analysis was performed to determine the phase distribution in an entire LRM particle. The technique involves recording convergent beam electron diffraction patterns in a two-dimensional grid of electron probe positions. Data processing can be used to provide information about material properties, including phase, orientation, strain and electromagnetic field distribution²⁷. The representative 4D-STEM results in Fig. 1b show a core/shell distribution of phases. The core (interior) and shell consist of $\text{O}3'$ and S phases, respectively, as expected from synthesis. High-angle annular dark-field

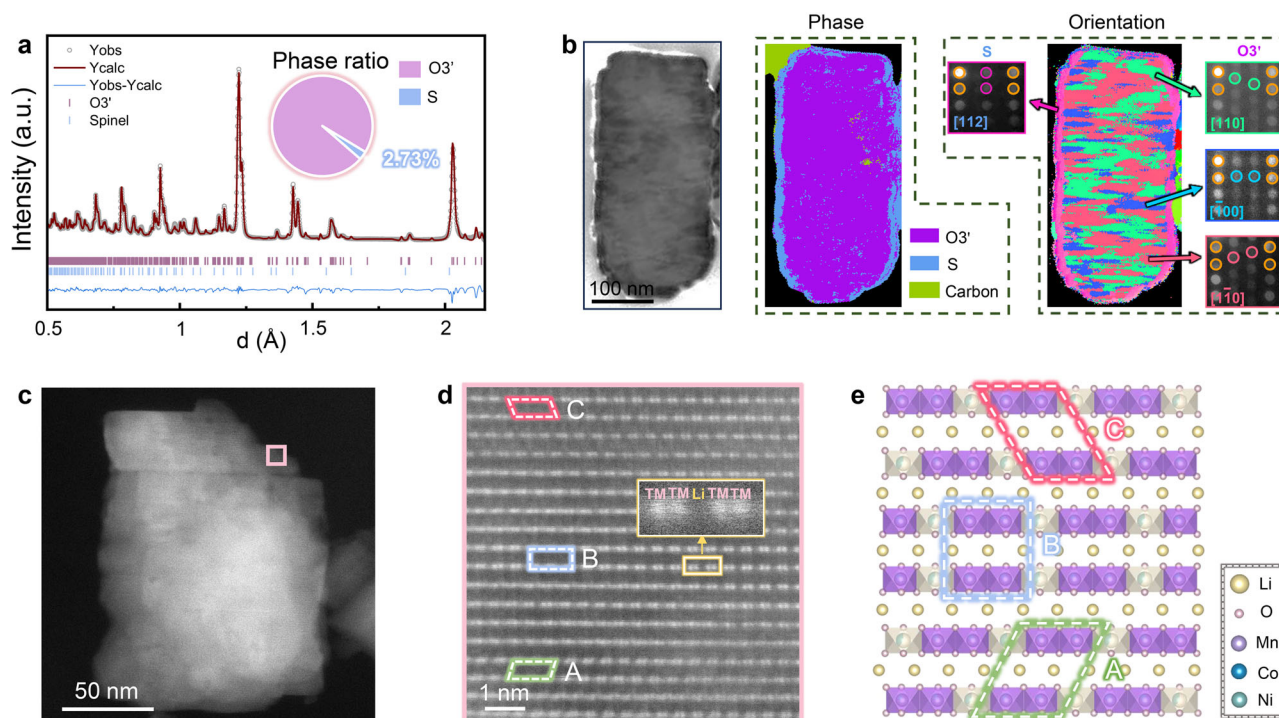


Fig. 1 | Initial structure of the LRM material. **a** NPD and Rietveld refinement analysis of pristine LRM powder. The inset sector plot shows the phase fraction distribution. **b** 4D-STEM results. Left to right: Virtual bright-field image, phase map and orientation map of a pristine LRM nanoparticle. Purple regions in the phase map denote the $\text{O}3'$ phase, blue regions the spinel phase and green regions amorphous C domains. **c** Low-magnification HAADF-STEM image of a pristine LRM

particle. **d** High-resolution HAADF-STEM image of the marked area in (c), showing the atomic arrangement in the pristine LRM cathode, which exhibits structural domains in the $\text{O}3'$ phase. The areas marked A (green), B (blue) and C (pink) correspond to domains projected along $[110]$, $[\bar{1}00]$ and $[\bar{1}\bar{1}0]$, respectively. **e** Schematic diagram of the $\text{O}3'$ phase, showing different types of structural domains.

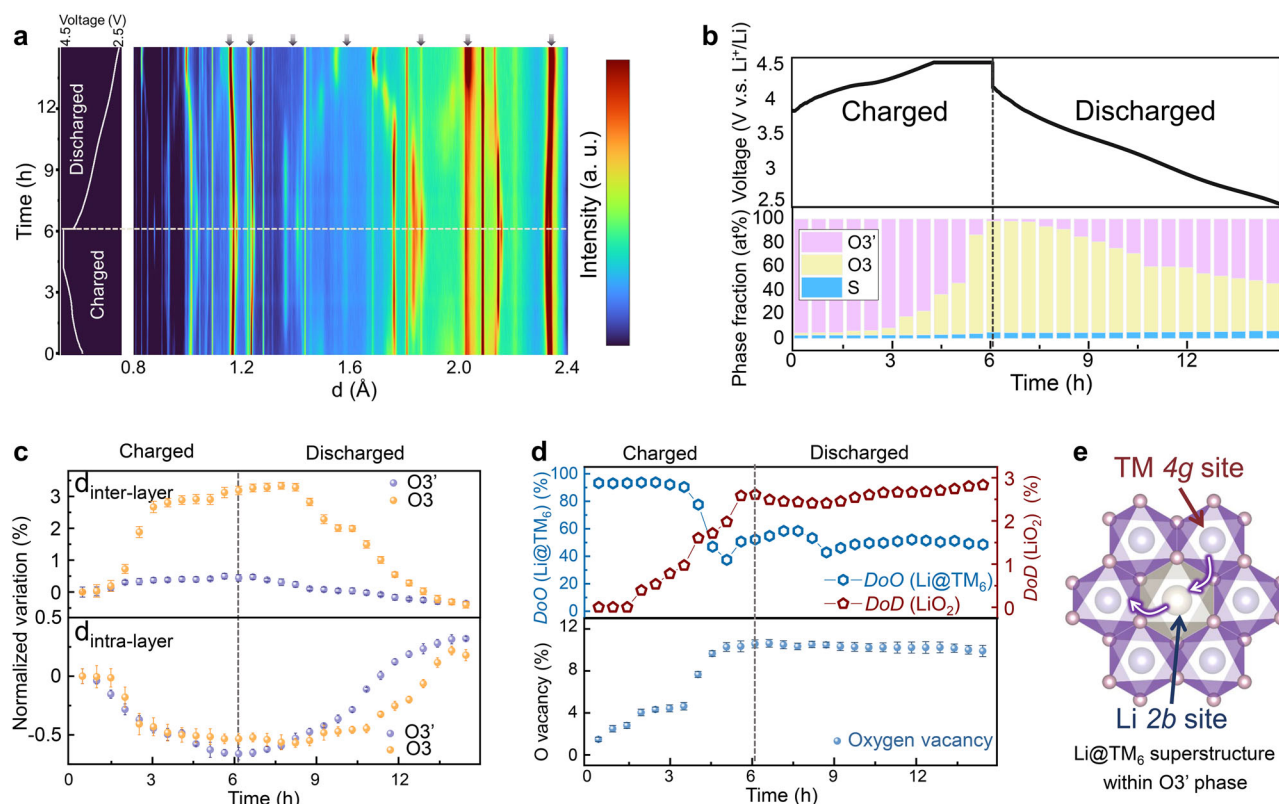


Fig. 2 | Structural evolution of the LRM cathode during the first cycle. **a** First charge/discharge curves of a graphite || LRM pouch cell and corresponding surface contour plot recorded using *operando* neutron diffraction. Contributions of LRM are marked by arrows. **b** Phase fraction evolution during the first cycle. Purple: O3'; yellow: O3; blue: spinel. **c** Values of $d_{\text{inter-layer}}$ and $d_{\text{intra-layer}}$ for the O3' and O3 phases in the LRM cathode obtained from Rietveld refinement as a function of cycling time. (In the hexagonal crystal system, $(003)_{\text{O3}}$ is equivalent to $(001)_{\text{O3}}$ in the monoclinic

system. Therefore, $d_{\text{inter-layer}}$ corresponds to $d_{(003)_{\text{O3}}}$ and $d_{(001)_{\text{O3}}}$. Similarly, $(100)_{\text{O3}}$, $(010)_{\text{O3}}$ and $(110)_{\text{O3}}$ are equivalent to $(131/3)_{\text{O3'}}$, $(\bar{1}31/3)_{\text{O3'}}$ and $(202/3)_{\text{O3'}}$, respectively. Therefore, $d_{\text{intra-layer}}$ corresponds to $[d_{(100)_{\text{O3}}} + d_{(010)_{\text{O3}}} + d_{(110)_{\text{O3}}}] / 3$ in the O3 phase and to $[d_{(131/3)_{\text{O3'}}} + d_{(\bar{1}31/3)_{\text{O3'}}} + d_{(202/3)_{\text{O3'}}}] / 3$ in the O3' phase. **d** Calculated ratio of DoO (Li@TM_6), DoD (LiO_2) and O vacancy plotted as a function of cycling time. **e** Schematic diagram of the Li@TM_6 superstructure in the O3' phase, in which Li and TM at the TMO_2 slabs occupy 2b and 4g Wyckoff sites, respectively.

(HAADF) STEM results confirm that the core/shell interface lies along $[010]_{\text{O3}}/[110]_{\text{S}}$, with the spinel shell varying in thickness from 2 to 5 nm (Supplementary Fig. 1). O-K edge electron energy-loss spectroscopy (EELS) shows an increase in pre-edge peak intensity from the shell to the interior (Supplementary Fig. 4a, b), suggesting a change in local O environment²⁸. The Mn- $L_{2,3}$ edge shows a reduced Mn oxidation state in the shell, as evidenced by an increase in L_3/L_2 ratio (Supplementary Fig. 4c, d)²⁹, in agreement with the presence of a spinel layer.

Supplementary Fig. 5 shows an O3' phase orientation map, which highlights the presence of structural domains in the LMR oxide^{30,31}. The domains are also revealed in the high-resolution HAADF-STEM shown in Fig. 1d. The bright–bright–dark contrast corresponds to TM–TM–Li ordering, which is characteristic of the O3' phase (see the inset to Fig. 1d). Three types of stacking of 'bright–bright–dark' contrast along $[001]_{\text{O3'}}$ form structural domains that are denoted A (green), B (blue) and C (pink). More details could be found in Supplementary Fig. 5a–c. Additional disordered structures visible in Fig. 1e show a diagrammatic representation of the types of structural domains in the O3' phase, which are in agreement with the observations.

Phase evolution upon charge/discharge cycling

The structural evolution of the LRM oxide, which involves phase transitions, Li^+ and TM^{n+} migration and the release of O, poses severe challenges for conventional characterization methods. Whereas significant efforts have been made to study miniaturized coin half cells, the true conditions in a pouch cell are more complex, especially in an operational environment. Neutron diffraction offers sensitivity to light

elements and the ability to distinguish elements with similar atomic numbers and different phases. The setup of the *operando* neutron diffraction experimental device used here is shown schematically in Supplementary Fig. 6a. In this configuration, incident neutrons interact with a pouch cell during a charge/discharge process, and scattered neutrons are captured by annular detectors. A well-designed graphite || LRM pouch cell was prepared with 16 electrode layers and a gasbag (Supplementary Fig. 6b). The designed parameters of pouch cell are shown in Supplementary Fig. 7. The lattice parameters of the uncharged LRM oxide in the pouch cell are similar to those in the pristine powder (Supplementary Table 2), confirming that there is negligible influence from cell assembly and activation.

Figure 2a shows initial charge/discharge curves and two-dimensional plots of the evolution of neutron diffraction patterns as a function of time. The peaks marked by arrows are reflections from the LRM cathode. The pouch cell underwent a formation process before cycling (Supplementary Fig. 8). Then, it was initially charged to 4.5 V at a current of 500 mA ($1\text{C} \approx 4000\text{ mA}$), followed by a constant voltage charge at 4.5 V. It was then discharged to 2.5 V at a current of 500 mA. Despite some overlap of the reflections, in particular in the low- d region, most of the reflections from the cathode and anode can be distinguished (Supplementary Fig. 9). Neutron diffraction patterns recorded from the pouch cell in the uncharged and fully-charged (4.5 V) states were analyzed to understand the transformations of the cathode material during the charge/discharge processes. Refined patterns for the two states are shown in Supplementary Fig. 10. The refinement considered layered structures of the O3' phase, the O3 phase (space group: $R\bar{3}m$) and the

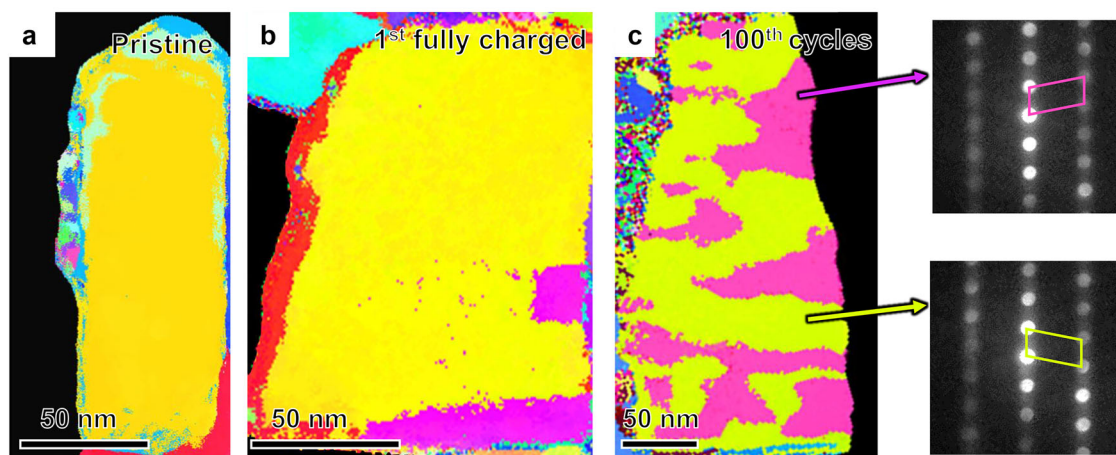


Fig. 3 | LRM structure evolution viewed along the $\langle 100 \rangle_{O3}$ projection. a–c In-plane orientation mapping of (a) a pristine particle, **b** a particle after a first charge to 4.5 V and **c** a particle after 100 cycles. The diffraction patterns were obtained from the purple and yellow areas in (c), which have mirror symmetry. The

corresponding diffraction patterns of yellow and purple areas in (b) are similar to those in (c). Note that in the pristine state, the particle is dominated by the O3' phase; its orientation relationship with O3 is given in Supplementary Fig. 5.

spinel structure. The goodness of fit confirms the precision of the calculated lattice structure of the LRM oxide.

Figure 2b shows the variation in phase fraction during the first cycle. During charging, the dominant O3' phase decreases gradually and almost completely transforms to the O3 phase at 4.5 V, as confirmed using phase mapping and atomic-resolution STEM (Supplementary Fig. 11). This transition is in agreement with previous findings³². However, the reverse transition is limited, with only half of the O3 phase returning to the O3' phase after discharging. We also observed this phenomenon in HAADF-STEM image of the cathode at 2.5 V (Supplementary Fig. 12). This limited reversibility results from the evolution of the LRM cathode during the first cycle and associated alterations in lattice structure. The proportion of the S phase also increases (Fig. 2b). The width of the S shell is approximately 5–10 nm in a fully charged particle, as shown in Supplementary Fig. 11b. The reduced intensity of the pre-edge peak in O *K*-edge spectra (Supplementary Fig. 13a, b) suggests that O vacancies accumulate in the S structure, in agreement with previous studies^{33,34}.

Figure 2c shows the variation in $d_{\text{intra-layer}}$ and $d_{\text{inter-layer}}$ in the O3' and O3 phases with cycling time. With the extraction of Li⁺ from the LiO₂ slabs, the shielding effect of electrostatic repulsion between adjacent TMO₂ slabs diminishes, increasing $d_{\text{inter-layer}}$ during charging. At the same time, $d_{\text{intra-layer}}$ contracts as a result of a reduction in ionic radius of the TMⁿ⁺ (most likely Ni²⁺ and Co³⁺; see Supplementary Fig. 13c, d), which are oxidized to higher valence states. Above 4.4 V, the triggered O redox reaction partly counteracts the shielding effect, decelerating the variations in $d_{\text{inter-layer}}$ and $d_{\text{intra-layer}}$ ³⁵. The increase in $d_{\text{inter-layer}}$ at the beginning of the discharge process may be attributed to sluggish diffusion kinetics in the pouch cell for LRM materials, which also affects variations in $d_{\text{intra-layer}}$. The smaller changes in $d_{\text{inter-layer}}$ and $d_{\text{intra-layer}}$ during discharge can be explained by O reduction.

In order to obtain further insight into the irreversibility of the structural evolution of the LRM cathode from the neutron diffraction data (see Fig. 2d), the degree of honeycomb Li@TM₆ ordering (*DoO*) in the TMO₂ slabs of the O3' phase is defined as follows:

$$DoO(\text{Li@TM}_6) = \frac{\text{Occ.}(\text{Li}, 2b)}{\text{Occ.}(\text{Li}, 2b) + 2\text{Occ.}(\text{Li}, 4g)} \times 100\%. \quad (1)$$

Figure 2e shows a fully-ordered Li@TM₆ superstructure in the O3' phase, in which only Li and only TM occupy 2b and 4g Wyckoff sites, respectively, i.e., *DoO* (Li@TM₆) = 100%. This situation corresponds to

the as-synthesized LRM in the pristine state. The degree of cation disordering (*DoD*) in the LiO₂ slabs of the O3' phase is defined by the percentage of TMs that migrate to 4h sites, as follows:

$$DoD(\text{LiO}_2) = \frac{2\text{Occ.}(\text{TM}, 4h)}{2\text{Occ.}(\text{TM}, 4h) + 2\text{Occ.}(\text{TM}, 4g) + \text{Occ.}(\text{TM}, 2b)} \times 100\%. \quad (2)$$

During charging, *DoD* (LiO₂) increases gradually, while *DoO* (Li@TM₆) remains almost constant, suggesting that TMs migrate from the TMO₂ to the LiO₂ slabs. When *DoD* (LiO₂) reaches ~1% (at 4.5 h), *DoO* (Li@TM₆) starts to decrease, suggesting that Li–TM reorganization takes place in the TMO₂ slabs. After charging to 4.5 V and during the entire discharging process, *DoO* (Li@TM₆) remains at ~50%, demonstrating a reduced degree of Li@TM₆ ordering (e.g., 4g site: TM_{0.75}Li_{0.25}–Li_{0.5}TM_{0.5}) in the O3' phase (see Fig. 2d). Disorder between Li and TM in the TMO₂ and LiO₂ slabs most likely accounts for the irreversible transition from the O3' phase to the O3 phase. The increase in *DoD* (LiO₂) occurs after the formation of O vacancies:

$$\text{O vacancy} = \text{O vacancy}(\text{O3}') \times \text{frac.}(\text{O3}') + \text{O vacancy}(\text{O3}) \times \text{frac.}(\text{O3}). \quad (3)$$

This behavior can be understood by the fact that O vacancies effectively lower the energy barrier associated with TM migration. The slight decrease in O vacancies during the discharge process suggests O reduction, as reported in the literature³⁵. Similar results with regard to O variation are obtained from soft X-ray absorption spectroscopy, as shown in Supplementary Fig. 14.

After 100 cycles (see Supplementary Fig. 15a), the LRM cathode comprises 72.02% of the O3 phase and 27.98% of the S phase (see Supplementary Fig. 15b and Supplementary Table 3), with no O3' phase detected after cycling. The thicker S shell (Supplementary Fig. 16a) results from the O3' → O3 → S phase transition, which is associated with irreversible Li loss and an accumulation of O vacancies (Supplementary Fig. 14). Atomic-resolution STEM imaging along $\langle 210 \rangle_{O3}$ (parallel to the O3' direction in Fig. 1d) reveals a completely disordered Li–TM arrangement (Supplementary Fig. 16b), without the characteristic O3' bright–bright–dark pattern that was present in the pristine sample.

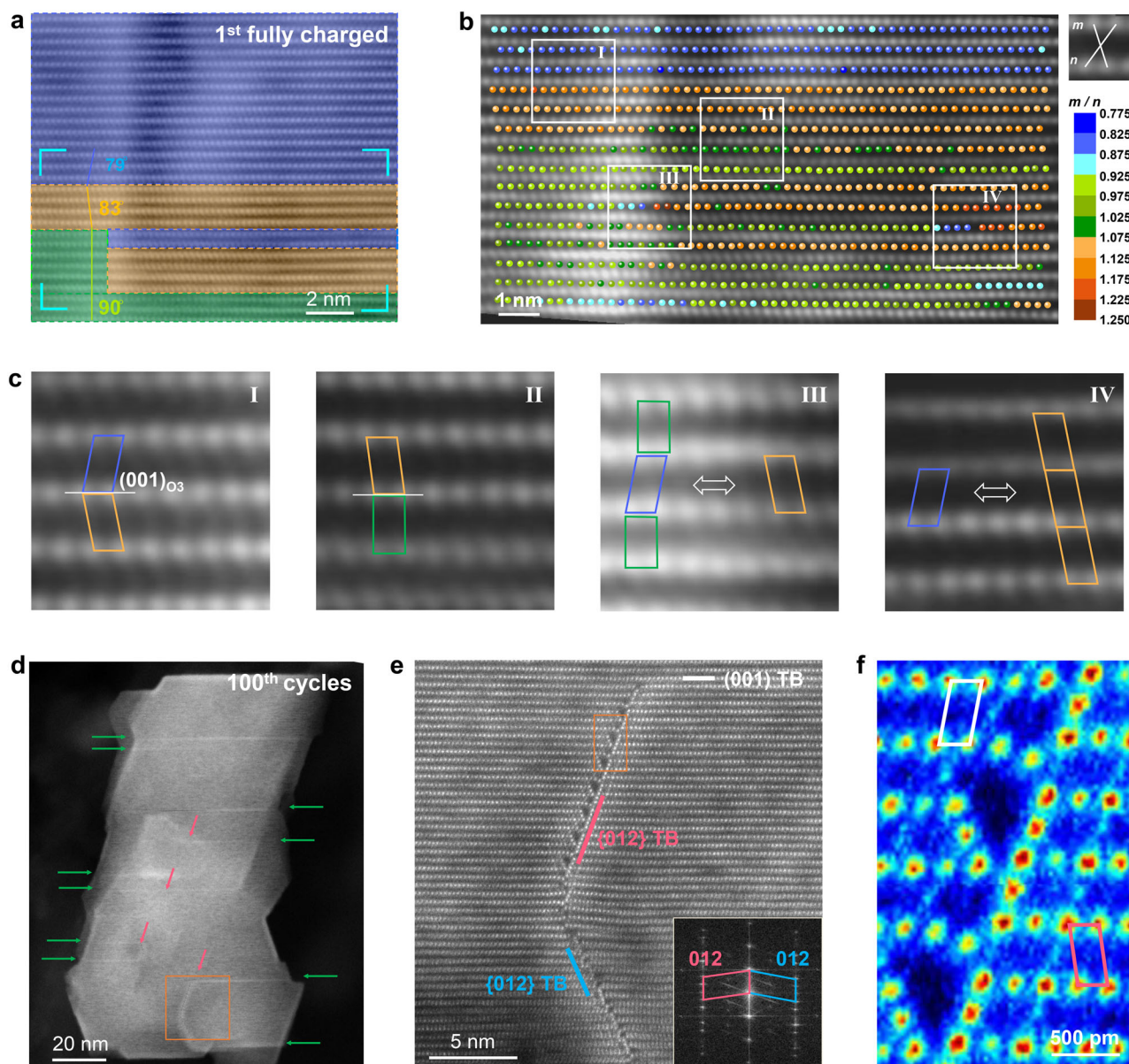


Fig. 4 | LRM structure after cycling. **a** Atomic-resolution image of a representative region viewed along $\langle 100 \rangle_{O3}$, showing changes to angles for the cathode charged to 4.5 V. **b** The unit-cell-by-unit-cell microstructural changes corresponding to the cyan area in **(a)**, defined by the ratio m/n , where m and n are the diagonal distances of the unit cell. **c** Magnified versions of areas I–IV in **(b)**. **d** HAADF-STEM image showing an overview of a representative particle after 100 cycles. The interlayer and intralayer twinning boundaries are marked by green and pink arrows. **e** Atomic-

resolution image of the area marked in **(d)**, showing the interlayer (001) coherent twinning boundary and intralayer {012} incoherent twinning boundaries. The inset shows an FFT of **(e)**, which confirms the presence of a twinning-like structure (see Supplementary Fig. 18). **f** High-resolution image of the area marked in **(e)**, showing pore-like microstructures resulting from the intralayer twinning-mediated frustration. The twinning variants are indicated by the white and pink frames.

Twinning-like structure evolution upon charge/discharge cycling

$\langle 210 \rangle_{O3}$ projections allow structural phases and domains associated with Li@TM_6 ordering to be identified using STEM techniques (refer to Supplementary Fig. 5a–d). In order to further study microstructures associated with the TM stacking layers, we focus on $\langle 100 \rangle_{O3}$ projections, along which Li and TM atoms line up (see Supplementary Fig. 5f, g). Figure 3 shows 4D-STEM orientation mapping of the microstructural evolution of LRM cathode particles upon cycling. Despite nanoscale intergrowth of $O3'$ phase domains associated with Li@TM_6 ordering (Fig. 1), the pristine sample has a single-crystal-like microstructure (Fig. 3a). After a first charge to 4.5 V, a twinning-like microstructure is observed (Fig. 3b). The corresponding diffraction patterns are similar to those in Fig. 3c recorded from LRM particles

after 100 cycles. The twinning structure generally develops further. The particles contain different orientations internally, with a significant fraction terminating in the particle, rather than extending across it. The results show that defects such as dislocations and stacking faults form primarily towards the end of the cycle. Diffraction patterns extracted from two areas (right part of Fig. 3c) have mirror symmetry, which is consistent with twin-like structures in the purple and yellow regions. As the resolution of the 4D-STEM technique was ~ 2 nm, finer structures could not be resolved.

Figure 4a, b shows low-magnification and magnified HAADF-STEM images of an LRM nanoparticle as it was initially charged to 4.5 V. The (acute) angles between the TM stacking layers vary, forming twinning-like structures (marked in blue and orange). The angles in neighboring variants are $\sim 79^\circ$ and $\sim 83^\circ$. Regions of $O1$ -type structure, which are

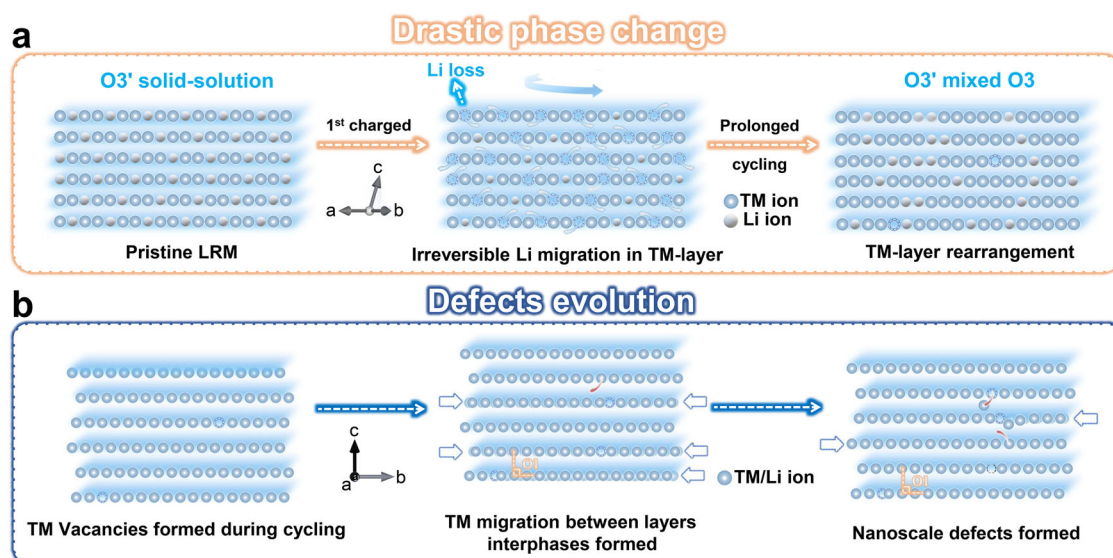


Fig. 5 | Evolution process of nanoscale defects and TM migration. a Schematic diagram of phase evolution. **b** Schematic diagram of the correlation between defects and TM migration.

identified by a 90° angle between the TM stacking layers (marked in green), typically have widths of below 2 nm (Supplementary Fig. 17a), which is beyond the present orientation mapping detection limit. Such structures have also been observed in delithiation Ni-rich cathodes³⁶. In comparison with an O1-type structure, twinning-like structures present greater challenges for Li⁺ accommodation in layer-structured Li-ion battery materials, hindering reversible Li⁺ intercalation³⁶.

Atomic-resolution detail from the area outlined in cyan in Fig. 4b was analyzed quantitatively. Image noise was removed using a non-linear algorithm, and atomic positions were measured using 2D Gaussian fitting³⁷. The ratio m/n between the two diagonals in each unit cell was determined based on the measured positions for tracing the structural variations. The result is shown in Fig. 4c. Two types of microstructures are highlighted: (1) A twinning-like structure (region I) and an O1/O3 boundary (region II), forming coherent interlayer microstructures with an (001)_{O3} habit plane. This twinning is called intralayer coherent twinning (refer to Supplementary Fig. 18). The m/n ratio in region I is -0.85 and -1.15 for the blue and magenta variant, respectively; (2) local structural frustrations in regions III and IV, which are indicative of intralayer microstructures and can be traced by extending the blue and magenta twinning variants in the magnified images (see the double-headed arrows). In this type of twinning structure, the {012}_{O3} twinning boundary (TB) is incoherent (so-called intralayer incoherent twinning). In the same layer, transitional interfaces that form a quasi-twinning structure are not continuous. When adjacent twinning variants meet at TB, structural frustration forms, as illustrated in Supplementary Fig. 18. Similar structures were previously observed in a Ni-rich cathode³⁶. The presence of intralayer frustration is indicative of nanoscale charge heterogeneity in fully-charged particles. More similar structures were observed, as shown in Supplementary Fig. 17. Mapping of interlayer spacings (Supplementary Fig. 17b) shows an uneven lattice distribution after charging, indicating a non-uniform delithiation process, with expansion and contraction of the interlayers. Strain measurement using geometric phase analysis reveals significant strain accumulation in the vicinity of a frustrated interface (Supplementary Fig. 19)³⁸. In subsequent cycles, such frustrated structures may be prone to strain relaxation, leading to structural failure.

The atomic structures in the LRM cathode after 100 electrochemical cycles are shown in Fig. 4d–g. Both interlayer and intralayer microstructures have developed further. Similarly to Fig. 4b, the

interlayer microstructures maintain their coherence between neighboring twinning variants, while the intralayer interfaces expand in the {012}_{O3} habit planes. The density of intralayer interfaces (Supplementary Fig. 20, Supplementary Table 4) is ~5 per particle. Strikingly, pore-like structures form at the {012}_{O3} twinning interface due to the expansion of local intralayer frustrations, leading to lattice bending and reduced atomic connectivity, as revealed in Fig. 4e, f. The Fast Fourier Transform (FFT) of the high-resolution image reveals a twinning-like structure (Fig. 4g). The formed pore-like interface microstructures, which resemble trenches, are believed to block Li⁺ diffusion during charge-discharge operations, reducing Li delithiation–lithiation and resulting in fading of battery capacity with cycling. Additionally, the EELS and EDS measurements were conducted in the defect and normal areas. The spectrum in Supplementary Fig. 21 showed that the Mn concentration in the defect region is lower than that in the normal region, and the valence of Mn in the defect region is Mn³⁺, while it is Mn^{3.5+} in the normal region. These results revealed the dissolution and migration of Mn in the defect area during cycling, which is consistent with the results from the neutron diffraction.

Discussion

Based on our experimental observations, the phase evolution of LRM cathodes is shown schematically in Fig. 5a. During charging, with Li⁺ extraction from the Li layers, Li⁺ in the TM layers also migrate to the Li layers. At high voltage, anion oxidation drives rearrangement in the TM layers, which contains Li vacancies, leading to the formation of O clusters that facilitate oxidation of O²⁻ into O₂²¹. This is an irreversible redox pathway for O, resulting in voltage hysteresis during discharge. Therefore, minimizing or preventing the rearrangement of TMⁿ⁺ within the TM layers can effectively address the issue of voltage hysteresis during electrochemical processes. In the context of Li–Mn-based sodium-ion cathodes, optimizing the ordered superlattice of Li and TM within the TM layers has proven to be an effective strategy for suppressing TM rearrangement, thereby reducing voltage hysteresis²¹. With Li⁺ reinsertion into the Li layers during discharge, some of them migrate back into the TM layers. However, as a result of the mixed distribution in the TM layers, the ordered structure of the O3' phase is disrupted, resulting in partial transformation of the O3' phase into the O3 phase. This transformation proceeds irreversibly during continued cycling, reducing the cell capacity. Nevertheless, this phase transition may not be the primary reason for performance degradation, as

cathodes with pure S or O3 phases still have some capacity¹⁴. Instead, expansion of the intralayer microstructures is most likely to be responsible for electrochemical performance decay.

As shown in Fig. 5b, a large number of TM and O vacancies form in the TM layers, together with irreversible migration of Li and the release of O. Lithium, transition metal, and oxygen vacancies may result in localized vacancy loops³⁹, which develop into the observed defects extending over the whole nanoparticle. According to the previous report, the dislocations formed more readily in the Li-rich cathode as compared with a classical layered oxide³⁹. Similarly, we posit that interlayer slips of TM layers occur during electrochemical cycling, forming two types of twinning-like structures: one is interlayer coherent twinning, and the other is intralayer incoherent twinning, and O1/O3 boundaries. The structural frustration forms when these twinning variants meet at the twinning boundary. As cycling progresses, the interlayer twinning-like structures maintain their coherence between neighboring twinning variants, while the intralayer TBs expand in the {012}_{O3} habit planes. More prominent frustration is evidenced by the formation of local pore-like microstructures (or trenches) at the {012}_{O3} TBs, as shown in Fig. 4 and Supplementary Fig. 22. The formation of pore-like interface microstructures reduces atomic connectivity and hinders Li⁺ diffusion from the bulk to the surface. We propose that the irreversible migration of TMⁿ⁺ plays an important role in the structure and performance failure in LRM oxides. Introducing pinning TMs above central Li⁺ sites in the Li@TM₆ honeycomb superstructure might be an effective approach to stabilize Li⁺ within the TM layers and prevent interlayer migration, thereby achieving low voltage and capacity fade⁷.

Surface reconstruction is also a crucial factor for material failure⁴⁰. Our work considers surface effects by modifying the particle surfaces with a spinel layer to reduce O release and to minimize the generation of side reactions during cycling. Although the surface spinel phase thickens during extended cycling, it does not prevent material failure due to changes in inner bulk structure and degradation in material performance results primarily from intrinsic structural changes. Our findings suggest that coating or surface modification methods may help to inhibit surface degradation, but are likely to be insufficient to prevent capacity fade because nanoscale defect formation can proceed from the particle interior. Modification of the bulk structure, for example by anchoring TMⁿ⁺ in the TM layers to suppress their inter-/intra-layer migration, should be considered to stabilize the structures of Li-rich cathodes for improved electrochemical performance. The above discussion further guided the optimization of Li-rich oxide cathodes, which was provided in Supplementary Fig. 23.

In summary, a combination of STEM and *operando* neutron diffraction techniques has been used to reveal the relationship between microstructure and performance in LMR cathodes across different length scales. Synthesized pristine LRM particles are shown to comprise a solid solution, with Li@TM₆ ordering based on C2/m symmetry (O3' type) surrounded by a thin spinel shell. It transitions from an ordered monoclinic phase to a disordered rhombohedral phase as a result of irreversible Li⁺ migration and TMⁿ⁺ rearrangement during cycling. During initial cycling, the irreversible extraction of Li⁺ from TM layers leads to the formation of the interlayer (001) twinning-like structures and local intralayer frustrations formed in the material. During subsequent extended cycles, the intralayer frustrations further develop into pore-like structures along {012} twinning boundaries in the bulk of the particles, with the continuous loss of Li⁺ and the migration of TMⁿ⁺ within the layers. These defects obstruct channels for Li-ion transport within the layers, causing a deterioration in material performance. These observations provide a perspective on material failure mechanisms in layered high-energy cathodes and emphasize the importance of intrinsic modification methods for stabilizing their internal structures beyond surface modification.

Methods

Material synthesis

The cathode precursor Mn_{2/3}Co_{1/6}Ni_{1/6}CO₃ was synthesized by a co-precipitation method. First, 2.0 mol/L MnSO₄·4H₂O (Aladdin, 99.9%), NiSO₄·6H₂O (Aladdin, 99.9%) and CoSO₄·7H₂O (Aladdin, 99.9%) solutions were stirred in the reactor. Meanwhile, 2.0 mol/L Na₂CO₃ (Aladdin, 99.9%) and NH₄OH solution (Aladdin, 500 mg/L) were added to the reactor separately. The stirring temperature was kept at 60 °C at a fixed pH value of 7.8. The precursor powders were obtained after washing several times with deionized water and dried in a vacuum at 80 °C for 12 h. The precursor was then well ground with Li₂CO₃ (Aladdin, 99.9%) (5% excess). Subsequently, the obtained mixture was transferred to a furnace, calcined at 480 °C for 5 h and heated to 850 °C for 12 h in air. The untreated Li_{1.2}Mn_{0.54}Ni_{0.13}Co_{0.13}O₂ (u-LRM) was obtained. Then, the synthesized LRM with a thin spinel-layer product was obtained after re-sintering for 3 h at a heating speed of 2 °C min from room temperature to 400 °C in an Ar atmosphere. The synthesized samples were stored in an Ar-filled glovebox (Mikrouna Super 1220) with O₂ and H₂O contents of below 0.01 ppm.

Half-cell preparation

The synthesized u-LRM or LRM material, which served as the active material for the half-cell cathode, was mixed with acetylene black (C45 Conductive Carbon Black, TIMCAL) and poly(vinylidene fluoride) (PVDF) (Aladdin, K30) in the ratio 8:1:1 (wt%) in N-methyl-2-pyrrolidone (NMP) (Aladdin, 99.5%) solvent to form a homogeneous slurry. This slurry was uniformly coated on a 40-μm-thick aluminum foil and dried in an oven at 80 °C for 2 h. The preliminarily dried electrode sheet was cut into circular pieces of diameter 12 mm, ensuring a loading of active material per single sheet of at least 2 mg cm⁻². These electrode sheets were placed in a vacuum oven at 110 °C for 12 h to remove the solvents and any residual moisture. The dried electrode sheets were stored in an Ar-filled glovebox (Mikrouna Super 1220) with O₂ and H₂O contents of below 0.01 ppm. The anode of the half-cell utilized a pure Li metal foil (16 mm diameter, 0.6 mm thickness, 99.9% purity) and a polypropylene separator (25 μm, Celgard 2500). The electrolyte utilized was 1 M LiPF₆ dissolved in a mixed solution of 1,1,2,2-tetrafluoroethyl-2',2',2'-trifluoroethyl, methyl (2,2,2-trifluoroethyl) carbonate and fluoroethylene carbonate (2:6:2, wt%). The assembly of coin-type half-cells (2032) was performed in the same glovebox.

Pouch cell preparation

The LRM cathode material was dispersed homogeneously in NMP with acetylene black and PVDF in a precise ratio of 9:0.5:0.5 (wt%) to form a well-mixed slurry. This slurry was coated onto Al foil (145 mm × 75 mm). The graphite anode material was dissolved in NMP, incorporating acetylene black and PVDF in the same ratio, to generate a slurry that was coated onto Cu foil (145 mm × 75 mm). The capacity of the anode exceeded that of the LRM cathode. Pouch cell assembly was carried out meticulously in a glovebox, including integration of the cathode, anode, separator and electrolyte. In order to enhance the loading of the active materials and to optimize the neutron diffraction patterns, the cathode and anode materials were coated uniformly on both sides of the Al foil and Cu foil. The resulting cell configuration comprised 16 pieces of dual-sided LRM cathode and graphite anode. A Celgard separator was used to alternate coverage of the anode and cathode on each side. The electrolyte utilized was the same as for the half cell. The assembly of the pouch cell was performed in the same glovebox.

Electrochemical tests

Half cell: Cyclic voltammetry (CV) measurements were conducted using an OCTOSTAT200 electrochemical workstation (IVIUM Instrument) in the voltage range 2–4.8 V versus Li⁺/Li at room temperature with a scan rate of 0.1 mV s⁻¹. Galvanostatic charge/discharge (GCD) tests were carried out on a Landt Instruments battery cycler at specific

current densities ($1\text{ C} = 250\text{ mA g}^{-1}$) in the voltage window 2.0–4.8 V versus Li^+/Li at 30°C .

Pouch cell: The pouch cell was designed with a standard capacity of 4 Ah. Initially, the as-prepared pouch cell underwent a formation process, charging to 4.5 V at increasing currents of 250 mA, 500 mA and 1000 mA, in order to ensure complete electrolyte infiltration into the cathode, anode and separator of the pouch cell. Subsequently, the activated pouch cell was used for *operando* neutron diffraction experiments. The final analysis of the failed LRM structure was conducted based on the pouch cell after 100 cycles at 4000 mA in the voltage range 2.5–4.5 V.

Neutron powder diffraction and *operando* neutron diffraction

Neutron powder diffraction experiments were carried out on the time-of-flight (TOF) diffractometer Multi-Physics Instrument (MPI) at China Spallation Neutron Source (CSNS), Dongguan, China⁴¹. Charge and discharge tests of the pouch cell were conducted using a battery cycler (Landt Instruments) with a constant current of 400 mA for the first cycle. TOF neutron diffraction data for *operando* pouch cell analysis were acquired on the General Purpose Powder Diffractometer (GPPD) at CSNS⁴². An incident neutron beam with a wavelength band ranging from 0.1 to 4.9 \AA was used. Real-time neutron diffraction data were collected while the pouch cell underwent charge and discharge processes. The crystal structures of the electrodes were determined through Rietveld refinement using the FullProf program⁴³.

HAADF and 4D-STEM data collection

In order to prepare samples for transmission electron microscopy, the electrodes were washed after cycling using dimethyl carbonate and dried in an Ar-filled glovebox. Both the pristine cathodes and the cathodes after cycling were ultrasonicated in ethanol for 15 min and dispersed on Cu TEM grids for characterization.

Electron microscopy techniques, including HAADF imaging and EELS, were performed at 200 kV on an FEI Titan G2 ChemiSTEM 80–200 transmission electron microscope equipped with a high-brightness field emission gun and a probe spherical aberration (Cs) correction system. Atomic-resolution HAADF-STEM images were acquired in STEM mode using a high-angle annular dark-field detector. The convergence semi-angle for HAADF imaging was $\sim 25\text{ mrad}$, while the collection semi-angle was $\sim 70\text{--}200\text{ mrad}$. EEL spectra were acquired in STEM mode. The convergence semi-angle was the same as for HAADF imaging.

4D-STEM experiments were conducted on a Tescan Tensor precession-assisted 4D-STEM microscope, which can perform near-real-time analysis and processing of 4D-STEM data, using a convergence semi-angle of 1.5 mrad , a beam current of 200 pA, a probe size of 1.5 nm , a diffraction size of 124.5 mrad and a precession angle of 0.8° . The electron probe was raster-scanned across NPs using a 2 nm step size. A diffraction pattern was recorded at each probe position using a high-performance hybrid-pixel direct electron diffraction camera (Dectris Quadro) with 512×512 physical pixels using 4-fold binning (128×128 pixels) and an exposure time of 3 ms for each pixel.

Synchrotron soft X-ray absorption spectroscopy

After the pouch cells had been charged and discharged to the target states, they were disassembled in the Ar-filled glovebox. The cathode components were extracted, subjected to thorough cleaning with a dimethyl carbonate (DMC) solution and dried. O K-edge absorption spectra were recorded meticulously from various LRM states in the RGBL beamline station at BESSY-II, Germany in fluorescence yield (FY) mode.

Data availability

Data that support the findings of this study are available from the corresponding author on request.

References

- Whittingham, M. S. Lithium batteries and cathode materials. *Chem. Rev.* **104**, 4271–4302 (2004).
- Li, M., Lu, J., Chen, Z. & Amine, K. 30 Years of lithium-ion batteries. *Adv. Mater.* **30**, 1800561 (2018).
- Wang, L., Liu, T., Wu, T. & Lu, J. Strain-retardant coherent perovskite phase stabilized Ni-rich cathode. *Nature* **611**, 61–67 (2022).
- Liu, J. et al. Recent breakthroughs and perspectives of high-energy layered oxide cathode materials for lithium ion batteries. *Mater. Today* **43**, 132–165 (2021).
- Liu, T. et al. Origin of structural degradation in Li-rich layered oxide cathode. *Nature* **606**, 305–312 (2022).
- Seo, D.-H. et al. The structural and chemical origin of the oxygen redox activity in layered and cation-disordered Li-excess cathode materials. *Nat. Chem.* **8**, 692–697 (2016).
- Luo, D. et al. A Li-rich layered oxide cathode with negligible voltage decay. *Nat. Energy* **8**, 1078–1087 (2023).
- Zuo, Y. et al. A high-capacity O2-type Li-rich cathode material with a single-layer Li_2MnO_3 superstructure. *Adv. Mater.* **30**, 1707255 (2018).
- Zuo, W. et al. Li-rich cathodes for rechargeable Li-based batteries: reaction mechanisms and advanced characterization techniques. *Energy Environ. Sci.* **13**, 4450–4497 (2020).
- Zuo, Y. et al. Regulating the potential of anion redox to reduce the voltage hysteresis of Li-rich cathode materials. *J. Am. Chem. Soc.* **145**, 5174–5182 (2023).
- Li, N. et al. Enabling facile anionic kinetics through cationic redox mediator in Li-rich layered cathodes. *ACS Energy Lett.* **5**, 3535–3543 (2020).
- Hao, Z. et al. Suppressing Bulk Strain and Surface O_2 Release in Li-rich cathodes by just tuning the Li content. *Adv. Mater.* **36**, 2307617 (2024).
- Kim, S. Y. et al. Inhibiting oxygen release from Li-rich, Mn-rich layered oxides at the surface with a solution processable oxygen scavenger polymer. *Adv. Energy Mater.* **11**, 2100552 (2021).
- Mohanty, D. et al. Unraveling the voltage-fade mechanism in high-energy-density lithium-ion batteries: origin of the tetrahedral cations for spinel conversion. *Chem. Mater.* **26**, 6272–6280 (2014).
- Song, J. et al. Entropy stabilization strategy for enhancing the local structural adaptability of Li-rich cathode materials. *Adv. Mater.* **35**, 2208726 (2023).
- Cui, C. et al. Structure and interface design enable stable Li-rich cathode. *J. Am. Chem. Soc.* **142**, 8918–8927 (2020).
- Guo, W. et al. Enhancing cycling stability in Li-rich Mn-based cathode materials by solid-liquid-gas integrated interface engineering. *Nano Energy* **97**, 107201 (2022).
- Kim, S., Cho, W., Zhang, X., Oshima, Y. & Choi, J. W. A stable lithium-rich surface structure for lithium-rich layered cathode materials. *Nat. Commun.* **7**, 13598 (2016).
- Ye, Z. et al. A simple gas–solid treatment for surface modification of Li-rich oxides cathodes. *Angew. Chem. Int. Ed.* **60**, 23248–23255 (2021).
- Yang, J. et al. Suppressing voltage fading of Li-rich oxide cathode via building a well-protected and partially-protonated surface by polyacrylic acid binder for cycle-stable Li-ion batteries. *Adv. Energy Mater.* **10**, 1904264 (2020).
- House, R. A. et al. The role of O_2 in O-redox cathodes for Li-ion batteries. *Nat. Energy* **6**, 781–789 (2021).
- Csernica, P. M. et al. Persistent and partially mobile oxygen vacancies in Li-rich layered oxides. *Nat. Energy* **6**, 642–652 (2021).
- House, R. A. et al. First-cycle voltage hysteresis in Li-rich 3d cathodes associated with molecular O_2 trapped in the bulk. *Nat. Energy* **5**, 777–785 (2020).
- Huang, J. et al. Inhibiting collective cation migration in Li-rich cathode materials as a strategy to mitigate voltage hysteresis. *Nat. Mater.* **22**, 353–361 (2023).

25. Pearce, P. E. et al. Evidence for anionic redox activity in a tridimensional-ordered Li-rich positive electrode β - Li_2IrO_3 . *Nat. Mater.* **16**, 580–586 (2017).
26. Yin, C. et al. Structural insights into composition design of Li-rich layered cathode materials for high-energy rechargeable battery. *Mater. Today* **51**, 15–26 (2021).
27. Ophus, C. Four-dimensional scanning transmission electron microscopy (4D-STEM): from scanning nanodiffraction to ptychography and beyond. *Microsc. Microanal.* **25**, 563–582 (2019).
28. Li, L. et al. Hidden subsurface reconstruction and its atomic origins in layered oxide cathodes. *Nano Lett.* **20**, 2756–2762 (2020).
29. Tan, H., Verbeeck, J., Abakumov, A. & Van Tendeloo, G. Oxidation state and chemical shift investigation in transition metal oxides by EELS. *Ultramicroscopy* **116**, 24–33 (2012).
30. Jarvis, K. A., Deng, Z., Allard, L. F., Manthiram, A. & Ferreira, P. J. Atomic structure of a lithium-rich layered oxide material for lithium-ion batteries: evidence of a solid solution. *Chem. Mater.* **23**, 3614–3621 (2011).
31. Liu, H. et al. Unraveling the rapid performance decay of layered high-energy cathodes: from nanoscale degradation to drastic bulk evolution. *ACS Nano* **12**, 2708–2718 (2018).
32. Jiang, Y. et al. Revealing the thermodynamics and kinetics of In-plane disordered Li_2MnO_3 structure in Li-rich cathodes. *ACS Energy Lett.* **6**, 3836–3843 (2021).
33. Yu, L., Huang, Y., Han, Q., Zhu, J. & Lu, J. High cycling rate-induced irreversible TMO6 slabs glide in Co-free high-Ni layered cathode materials. *Adv. Funct. Mater.* **33**, 2301650 (2023).
34. Wang, R. et al. Constructing oxygen-deficient shell on Li-rich cathodes by spark plasma sintering for high-performance lithium-ion batteries. *Materials* **4**, 100195 (2024).
35. Zhou, Y. et al. Sufficient oxygen redox activation against voltage decay in Li-rich layered oxide cathode materials. *ACS Mater. Lett.* **3**, 433–441 (2021).
36. Wang, C. et al. Resolving complex intralayer transition motifs in high-Ni-content layered cathode materials for lithium-ion batteries. *Nat. Mater.* **22**, 235–241 (2023).
37. Du, H. A nonlinear filtering algorithm for denoising HR(S)TEM micrographs. *Ultramicroscopy* **151**, 62–67 (2015).
38. Hÿtch, M. J., Snoeck, E. & Kilaas, R. Quantitative measurement of displacement and strain fields from HREM micrographs. *Ultramicroscopy* **74**, 131–146 (1998).
39. Singer, A. et al. Nucleation of dislocations and their dynamics in layered oxide cathode materials during battery charging. *Nat. Energy* **3**, 641–647 (2018).
40. Yan, P. et al. Evolution of lattice structure and chemical composition of the surface reconstruction layer in $\text{Li}_{1.2}\text{Ni}_{0.2}\text{Mn}_{0.6}\text{O}_2$ cathode material for lithium ion batteries. *Nano Lett.* **15**, 514–522 (2015).
41. Xu, J. et al. Multi-physics instrument: total scattering neutron time-of-flight diffractometer at China Spallation Neutron Source. *NIM-A*. **1013**, 165642 (2021).
42. Chen, J. et al. The general purpose powder diffractometer at CSNS. *Physica. B*. **551**, 370–372 (2018).
43. Rodríguez-Carvajal J. Recent advances in magnetic structure determination by neutron powder diffraction. *Physica. B*. **192**, 55–69 (1993).

Acknowledgements

This work was supported financially by the National Key R&D Program of China (2020YFA0406203), Research Infrastructure Access in Nanoscience & Nanotechnology (RIANA) project, funded by the European Union (101130652), National Natural Science Foundation of China (No. 92472115 and No. 52072008), Guangdong Basic and Applied Basic Research Foundation (No. 2022B1515120070 and No. 2022A151510816), the Large Scientific Facility Open Subject of Songshan Lake, Dongguan,

Guangdong (No. FKFT2022A04) and the Major Science and Technology Infrastructure Project of Material Genome Big-Science Facilities Platform supported by the Municipal Development and Reform Commission of Shenzhen. The authors are grateful for the neutron beam time at MPI and GPPD granted by CSNS, Dongguan, China. Lunhua He, Jie Chen, Sihao Deng, Huaile Lu, Zhijian Tan, Feiran Shen and Yaoda Wu are thanked for technical assistance with the *operando* neutron diffraction experiments. Ziqin Jiao and Xiaoyu Gao are thanked for their support with the materials synthesis. Wen Yin, Yuanguang Xia and Juping Xu are thanked for technical assistance with the powder neutron diffraction experiments. The authors also thank the Tescan Tensor STEM team for their technical assistance during 4D-STEM experiments.

Author contributions

T. Y., M. Y., L. J. and Y. X. conceived the idea and designed the experiments. M. Y., R. W., Z. L. and J. W. prepared the pouch cell and conducted the electrochemical measurements. Z. H. and R. W. carried out the *operando* neutron diffraction measurements. M. Y. and Z. H. completed Rietveld refinement of all diffraction data. T. Y., P. L. and L. J. carried out 4D-STEM, STEM and EELS measurements and data analysis. M. Y., T. Z. and W. J. performed ex-situ sXAS tests and data analysis. T. Y., M. Y., Z. H., L. J., R. D. and Y. X. participated in the mechanism discussions. T. Y., M. Y., L. J., R. D. and Y. X. wrote the manuscript. All of the authors discussed the results and edited the paper.

Competing interests

The authors declare no competing interests.

Additional information

Supplementary information The online version contains supplementary material available at <https://doi.org/10.1038/s41467-025-61386-w>.

Correspondence and requests for materials should be addressed to Lei Jin or Yinguo Xiao.

Peer review information *Nature Communications* thanks Linsen Li, and the other, anonymous, reviewers for their contribution to the peer review of this work. A peer review file is available.

Reprints and permissions information is available at <http://www.nature.com/reprints>

Publisher's note Springer Nature remains neutral with regard to jurisdictional claims in published maps and institutional affiliations.

Open Access This article is licensed under a Creative Commons Attribution-NonCommercial-NoDerivatives 4.0 International License, which permits any non-commercial use, sharing, distribution and reproduction in any medium or format, as long as you give appropriate credit to the original author(s) and the source, provide a link to the Creative Commons licence, and indicate if you modified the licensed material. You do not have permission under this licence to share adapted material derived from this article or parts of it. The images or other third party material in this article are included in the article's Creative Commons licence, unless indicated otherwise in a credit line to the material. If material is not included in the article's Creative Commons licence and your intended use is not permitted by statutory regulation or exceeds the permitted use, you will need to obtain permission directly from the copyright holder. To view a copy of this licence, visit <http://creativecommons.org/licenses/by-nc-nd/4.0/>.

© The Author(s) 2025